

Light-Induced Transient Lattice Dynamics and Metastable Phase Transition in $\text{CH}_3\text{NH}_3\text{PbI}_3$ Nanocrystals

Ariel A. Leonard, Benjamin T. Diroll, Nathan C. Flanders, Shobhana Panuganti, Alexandra Brumberg, Matthew S. Kirschner, Shelby A. Cuthriell, Samantha M. Harvey, Nicolas E. Watkins, Jin Yu, Michael R. Wasielewski, Mercouri G. Kanatzidis, William R. Dichtel, Xiaoyi Zhang, Lin X. Chen, and Richard D. Schaller*



Cite This: *ACS Nano* 2023, 17, 5306–5315



Read Online

ACCESS |



Metrics & More



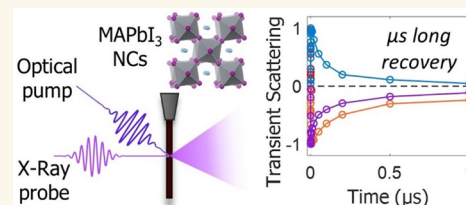
Article Recommendations



Supporting Information

ABSTRACT: Methylammonium lead iodide (MAPbI_3) perovskite nanocrystals (NCs) offer desirable optoelectronic properties with prospective utility in photovoltaics, lasers, and light-emitting diodes (LEDs). Structural rearrangements of MAPbI_3 in response to photoexcitation, such as lattice distortions and phase transitions, are of particular interest, as these engender long carrier lifetime and bolster carrier diffusion. Here, we use variable temperature X-ray diffraction (XRD) and synchrotron-based transient X-ray diffraction (TRXRD) to investigate lattice response following ultrafast optical excitation. MAPbI_3 NCs are found to slowly undergo a phase transition from the tetragonal to a pseudocubic phase over the course of 1 ns under 0.02–4.18 mJ/cm^2 fluence photoexcitation, with apparent nonthermal lattice distortions attributed to polaron formation. Lattice recovery exceeds time scales expected for both carrier recombination and thermal dissipation, indicating meta-stability likely due to the proximal phase transition, with symmetry-breaking along equatorial and axial directions. These findings are relevant for fundamental understanding and applications of structure–function properties.

KEYWORDS: methylammonium lead iodide, perovskite, transient X-ray diffraction, lattice dynamics, polaron, metastable state, photoinduced phase transition



Metal halide perovskites, available as thin films, single crystals, and colloidal nanocrystals (NCs), offer prospective utility in solar cells, light-emitting diodes (LEDs), and lasers.^{1,2} Highly desirable properties include tunable absorption, high photoluminescence quantum yield with narrow line widths, long carrier lifetimes, and amplified spontaneous emission.^{3–10} Uncertainty exists regarding how interband photoexcitation transiently changes the lattice as well as means by which structure evolution influences optoelectronic performance.¹¹ Optical excitation of bulk methylammonium lead iodide (MAPbI_3) yields excitons with low binding energies that can dissociate into free carriers, and unraveling the relationship between carrier behavior and crystal structure on ultrafast time scales is pertinent for both practical and fundamental purposes.^{12,13} Steady state measurements and density functional theory (DFT) calculations have suggested that photoexcitation can modify the crystal phase in MAPbI_3 through the manipulation of MA-I hydrogen bonds.^{14–17} Additionally, optical^{18–20} and physical^{14,21–23} studies performed on a variety of compositions have conveyed that lattice distortions in the form of large and small

polarons—wherein ionic nuclei within the vicinity of a charged carrier displace from their equilibrium lattice positions due to Coulombic interactions—form within picoseconds following excitation.²⁴ Such distortions yield dielectric screening of free carriers that can protect them from recombination as well as phonon or defect scattering, and may hold a key to long carrier lifetimes^{4,5} in addition to defect tolerance.²⁵

Thermal effects following light absorption also require consideration, as above-bandgap excitation subsequently yields intraband relaxation of hot carriers to the band edge, and background doping or elevated excitation fluence result in Auger recombination,²⁶ where an electron–hole pair non-radiatively recombines by exciting a third carrier that then

Received: July 13, 2022

Accepted: February 28, 2023

Published: March 14, 2023



ACS Publications

© 2023 UChicago Argonne, LLC,
Operator of Argonne National
Laboratory. Published by American
Chemical Society

5306

<https://doi.org/10.1021/acsnano.2c06950>
ACS Nano 2023, 17, 5306–5315

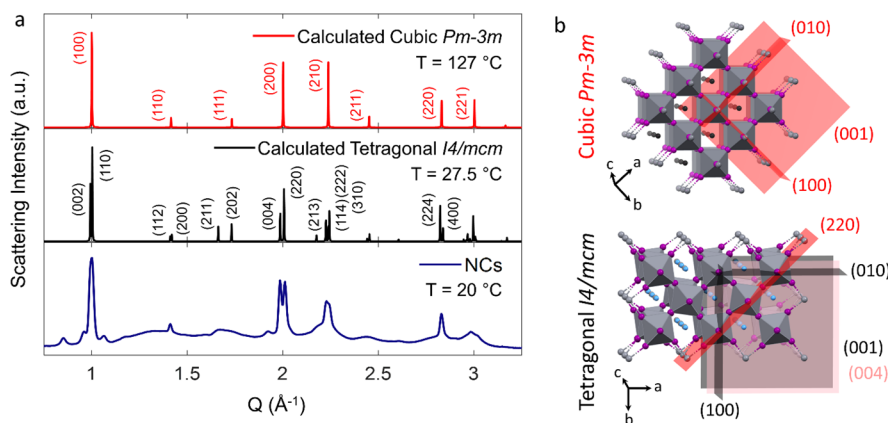


Figure 1. (a) Experimental diffraction patterns of room temperature MAPbI₃ NCs in the tetragonal phase (blue) and calculated diffraction patterns for MAPbI₃ bulk in the room temperature tetragonal (black) and elevated temperature cubic (red) phases. (b) Crystallographic representations of the tetragonal and cubic phases, generated from bulk powder diffraction patterns. The phase transition is characterized by rotation of the lead iodide octahedra along the *c*-axis. Crystallographic planes are labeled for each phase, where lattice parameters $a = b = c$ for the cubic phase and $a = b \neq c$ for the tetragonal phase. The unit cell axes as typically defined are tilted 45° to one another such that the tetragonal (110) and cubic (100) family of planes are parallel to one another, and the tetragonal (004) and (220) planes (shown in red) have reflections at a similar *Q*-value to the cubic (200) reflection.

deposits energy into the lattice. This is particularly relevant for MAPbI₃ because the phase transition from tetragonal to cubic symmetry²⁷ is thermally accessible at temperatures only moderately above room temperature (~ 60 °C in bulk crystal form^{28,29}). Low thermal conductivity in perovskites,^{30–32} coupled with known temperature and phase-dependence of optoelectronic properties such as charge carrier mobility³³ and optical bandgap,³⁴ thus motivates investigation of the photo-induced structural response of MAPbI₃ NCs.

Several recent studies have examined the first few nanoseconds following excitation in efforts to identify the nature of photoinduced lattice distortions in semiconducting materials; however, these have focused on other compositions^{11,19,21,35} or bulk MAPbI₃,²² with little investigation into MAPbI₃ NCs. Here, we use time-resolved X-ray diffraction (TRXRD) to measure the time scales associated with transient lattice changes in MAPbI₃ NCs. TRXRD uses pulsed optical excitation to set in motion lattice structural changes and X-ray probe pulses at different delay times to follow the evolution of the lattice response. We compare these time-resolved studies with static X-ray diffraction (XRD) studies at variable temperature to disambiguate thermal versus electronic influences. We find that a photoinduced phase transition from the tetragonal to a pseudocubic structure occurs over tens to hundreds of picoseconds and is likely both thermally and electronically driven. Initially after photoexcitation there is also a nonthermal expansion of the crystal lattice and lattice disordering attributed to large polaron formation. A slow return to tetragonal symmetry occurs over tens to hundreds of nanoseconds, which implicates a metastable state that persists even after the reported time scales for dissipation of thermal energy in NCs. This transient lattice configuration suggests that electron–hole pairs produced in the material facilitate distortions that in turn alter the crystal phase and, thereby, its physical properties.

RESULTS AND DISCUSSION

The measured diffraction pattern for room temperature, tetragonal phase MAPbI₃ NCs is shown in Figure 1a, along with the tetragonal (25 °C) and cubic (127 °C) patterns of

single-crystal MAPbI₃ calculated from available CIFs (CSD 968121 and CSD 968125).^{36,37} NCs with ~ 50 nm diameter, as analyzed via Scherrer broadening (see Table S1), were synthesized according to a modified procedure from Vybornyi et al.⁹ and suspended in dodecane. Although the tetragonal and cubic phases share many similar diffraction peak positions along the *Q*-axis, they also have distinctively different diffraction features;^{27,38} for example, at $Q \sim 2.0$ Å^{−1}, the tetragonal phase exhibits two diffraction peaks from the (004) and (220) planes, whereas the cubic phase has only a singular (200) reflection. Notably, the (211) peak at ~ 1.67 Å^{−1} is only consistent with the tetragonal phase and represents a convenient means to differentiate the crystal phases. Representations of the MAPbI₃ tetragonal and cubic phases, generated from the same single crystal diffraction data, are shown in Figure 1b. The lead ions are octahedrally coordinated by iodide ions with the methylammonium cations filling the interstitial sites. In the tetragonal phase, the lead-iodide octahedra are tilted about the *c*-axis; these rotate about the *c*-axis upon heating to produce a higher symmetry cubic structure above the phase transition temperature.^{29,39} The phase transition has previously been characterized as a first order transition in bulk MAPbI₃, although a recent study in CsPbBr₃ NCs has suggested that such phase transitions in lead halide perovskites may be caused by an increase in disorder according to the soft phonon model.⁴⁰

We first performed variable temperature XRD on colloidal NC suspensions in dodecane, as shown in Figure 2a–d. XRD patterns were collected over a temperature range from 25 to 175 °C in 25 °C increments. At 50 °C, the tetragonal to cubic phase transition becomes evident by the decreased intensity of the distinct tetragonal (211) peak (Figure 2b), which fully disappears by 100 °C. The phase transition is further indicated by emergence of cubic features. Over the same temperature range, the tetragonal (004) and (220) peaks, shown in Figure 2c, shift toward each other, corresponding to contraction along the (001) planes (shortening of the *c* lattice parameter) and expansion along the (110) planes (lengthening of the *a* lattice parameter) as the [PbI₆]^{4−} octahedra rotate, eventually merging into the cubic (200) peak. The three closely spaced

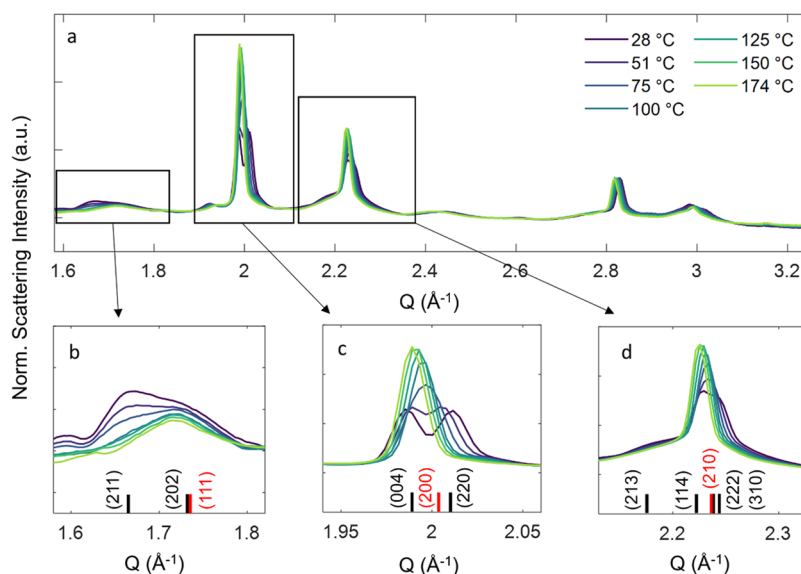


Figure 2. Variable temperature XRD for MAPbI₃ NCs over (a) an extended Q -range and (b–d) zoomed in regions highlighting the tetragonal (211), cubic (200), and cubic (210) peaks. Bulk peak positions are demarcated in black for tetragonal symmetry and red for cubic symmetry. Temperature was ramped from ~ 25 to ~ 175 °C in 25 °C increments. A phase transition from tetragonal to cubic symmetry is observed beginning at ~ 50 °C, apparent in the disappearance of the tetragonal (211) peak and the growth of the cubic (200) and (210) peaks.

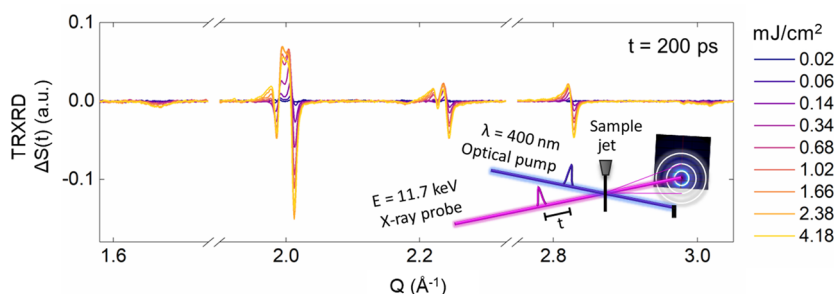


Figure 3. Transient diffraction patterns from TRXRD measurements over a range of excitation fluences at a delay time of $t = 200$ ps. Inset: schematic of the transient X-ray diffraction (TRXRD) setup at the APS. Experiments were conducted with both variable pump fluence at fixed delay time and variable delay time at fixed fluence to explore the power-dependent and dynamic responses of the NCs.

tetragonal (114), (222), and (310) peaks in Figure 2d are also observed transitioning to the single cubic (210) peak. Upon further heating above 100 °C, the cubic (200) and (210) peaks shift to a lower Q , indicating expansion of the cubic crystal lattice.

Next, we conducted transient X-ray diffraction (TRXRD) to determine NC structural response to optical excitation. These measurements utilized a pump–probe scheme, with a pulsed pump laser at 400 nm with a 10 kHz repetition rate and 1.6 ps (fwhm) pulse duration for above bandgap excitation, and a pulsed X-ray probe at 11.7 keV with 80 ps instrument response function for monitoring photoinduced structural changes via powder X-ray diffraction at variable delay times, t (schematic in Figure 3 inset). To highlight excitation-induced changes in the NC structure, we subtract the unexcited S_0 diffraction from the excited pattern $S(t)$ (pump on minus pump off) at each pump–probe delay time:

$$\Delta S(t) = S(t) - S_0 \quad (1)$$

In this way, contributions from the unexcited particles and solvent are removed, greatly enhancing sensitivity to the excited NC response.

Figure 3 displays $\Delta S(t)$ vs Q collected over a range of fluences (0.02–4.18 mJ/cm²) at a delay time of 200 ps. Transient signals are apparent at each of the Bragg peak positions with increasing intensity changes at progressively higher fluences, signifying that the optical excitation induces structural changes from the ground state lattice geometry. Panels a–c of Figure 4 show zoomed-in views of the same three Q ranges shown in Figure 2b–e. To determine whether TRXRD patterns could be attributed to thermal effects, we generated thermal difference patterns ($\Delta S(T)$) from the static variable temperature XRD, subtracting the room temperature measurement from higher temperature measurements:

$$\Delta S(T) = S(T) - S(28 \text{ °C}) \quad (2)$$

The thermal difference patterns for the same three Q -ranges presented in Figure 4a–c are shown in Figure 4d–f.

The TRXRD features point to a photoinduced phase transition from the tetragonal to a pseudocubic structure as well as additional structural distortions that static thermal measurements do not capture, suggesting a different origin likely owing to charge carriers. In the TRXRD patterns, a transition toward the cubic phase is implied by a decrease in

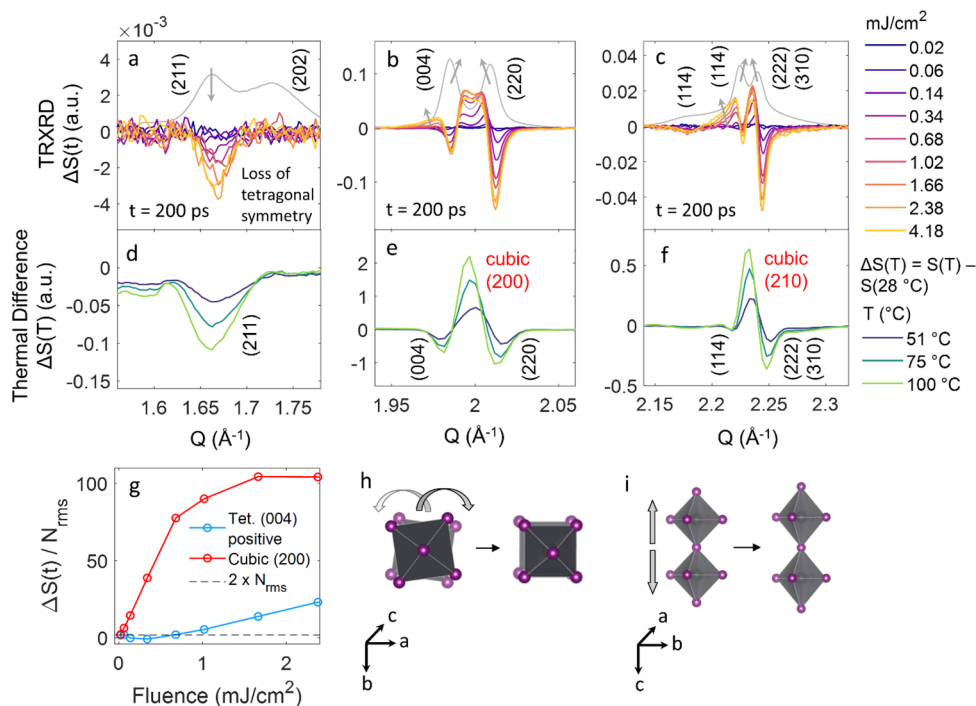


Figure 4. (a–c) Fluence-dependent transient diffraction patterns from TRXRD measurements for tetragonal (211), cubic (200), and cubic (210) peaks. Static diffraction patterns are shown in gray (arbitrary scaling) with arrows indicating the direction of photoinduced distortion. (d–f) Thermal difference patterns from variable temperature XRD measurements; the room temperature pattern was subtracted from higher temperature patterns to visualize thermal effects according to $\Delta S(T) = S(T) - S(28^\circ\text{C})$. Tetragonal reflections are labeled in black; cubic reflections are in red. (g) Fluence dependence of $\Delta S(t)$ divided by the RMS noise (N_{rms}) for the cubic (200) peak and the positive peak on the low Q side of the tetragonal (004) reflection (showing a higher fluence onset). (h and i) Representations of the $[\text{PbI}_4]^{4-}$ octahedra rotating from the tetragonal tilted to the cubic eclipsed conformation and the elongation of the Pb–I bond along the c -axis, respectively.⁴¹

intensity of tetragonal features in the form of negative TRXRD signals, and in the emergence of positive cubic features. In Figure 4a, the solely negative TRXRD signal at 1.663 \AA^{-1} corresponds to a decrease in the peak intensity of the tetragonal (211) reflection and loss of this phase. Similarly, in Figure 4b, we see negative features at 1.985 and 2.009 \AA^{-1} that convey the decreased intensity of the tetragonal (004) and (220) Bragg peaks.

In Figure 4b there are three positive features that arise, two of which appear similar to those observed from thermal effects and one of which differs. The emergent positive features on the high Q side of the (004) reflection and on the low Q side of the (220) reflection are indicative of a transition to a pseudocubic structure (represented in Figure 4h), as described for the variable temperature patterns in Figure 2c. The third positive feature on the low Q side of the tetragonal (004) peak is anomalous and represents an expansion of the (001) planes (Figure 4i). This expansion is compatible, however, with recent time-resolved Raman spectroscopy and theoretical simulations that have determined that electron polaron distortions of the Pb–I framework elongate the structure preferentially along the c -axis, a nonthermal effect arising from Coulombic interactions between the charged carrier and the polarizable ionic lattice.^{12,42} By plotting the maximum TRXRD intensity versus fluence of this feature in Figure 4g, we find that it only emerges at fluences above 0.68 mJ/cm^2 , which implies that the polarons modify the long-range structure only above a sufficiently high carrier density, although polaron formation is likely still occurring at lower fluences. This is in stark contrast to the cubic (200) feature on the high Q side of the (004) peak, which has a low fluence onset due to photoinduced rotation of

the lead-iodide octahedra causing an increase in symmetry. Similar behavior is observed in the Q -region shown in Figure 4d, where negative tetragonal reflections are superimposed upon a singular cubic (210) feature at 2.233 \AA^{-1} , along with a nonthermal positive peak that emerges on the low Q side of the tetragonal (114) reflection.

Additional key differences between the TRXRD patterns (Figure 4a–c) and the thermal difference patterns (Figure 4d–f) include the relative intensity of the negative tetragonal peaks to the positive pseudocubic peaks, which is much stronger in TRXRD. In the thermal difference patterns, the cubic peaks originate from the overall long-range ordering of the crystal structure as it adopts the higher symmetry phase. In the TRXRD patterns, the presence of the cubic features likewise implies phase ordering; however, the comparatively intense negative features point to additional deformation of the lattice by electron–hole pairs, either in the form of expansion, site disordering of the lead and iodide ions as a result of polaron formation, or rotational disorder of the lead iodide octahedra.^{22,40} The other key distinction is that the thermal difference patterns contain a single positive feature for each of the cubic (200) and (210) peaks, whereas in $\Delta S(t)$ there are multiple positive features. We suggest this may be due to the nonequilibrium nature of the transient structure, discussed in more detail below. In comparing the thermal difference patterns to the TRXRD patterns we note that the scales plotted here are in arbitrary units; however, intensity changes for thermal heating experiments were larger in comparison to TRXRD data, owing to the entire sample changing under equilibrium in the former as opposed to a photoexcited subpopulation in the latter.

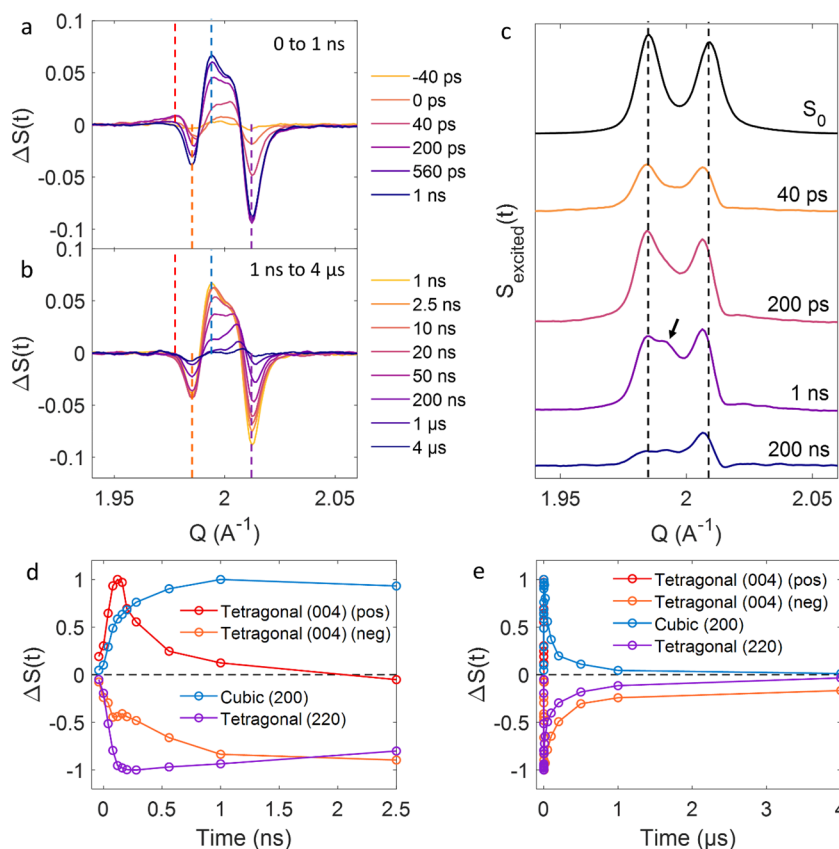


Figure 5. Dynamics of MAPbI₃ NC structural distortions and recovery. TRXRD patterns at delay times ranging from (a) -40 ps to 1 ns and (b) 1 ns to 4 μ s showing the MAPbI₃ NC dynamic response for the tetragonal (004), tetragonal (220), and cubic (200) reflections. The laser fluence was held constant at 2.4 mJ/cm². (c) Approximate scattering patterns of the excited NCs $S(t)$ at select time points. Scaled static pretime zero scattering pattern (S_0) is shown for reference, and dashed lines indicate static peak positions. The cubic peak most strongly appears at 1 ns, marked by an arrow. Kinetic traces are plotted for the (d) early and (e) late time domains using the maximum or minimum values of the peaks at each time point. Dashed lines in (a) indicate the peak position used to derive each of the kinetic traces.

TRXRD collected at a fixed excitation fluence of 2.4 mJ/cm² over a range of time delays (0 – 4 μ s) offers additional insights regarding the dynamic nature of the structural distortions and the ambient crystal phase recovery time. The resulting $\Delta S(t)$ vs Q patterns for the cubic (200) Q -region are shown in Figure 5a,b, with the early (0 – 1 ns) and late (1 ns– 4 μ s) time delay windows plotted separately, which correspond, respectively, to the rise and recovery of the transient signal. Additionally, Figure 5c shows an approximation of the scattering pattern $S(t)$ associated with the excited NCs, generated by scaling the static pattern, S_0 , to the TRXRD pattern at the tetragonal (220) Q -position with scaling factor a , and adding it to the $\Delta S(t)$ pattern:

$$S(t) = \Delta S(t) + a \times S_0 \quad (3)$$

Kinetic traces showing the evolution of specific tetragonal and cubic features are plotted in Figure 5d (0 – 2.5 ns) and 5e (0 – 4 μ s), with exponential fitting to estimate the time scales of the phase transition and recovery in Figures S12–S15.

Initially after photoexcitation (0 – 80 ps), we observe a pattern of neighboring positive and negative lobes in Figure 5a at the tetragonal (004) and (220) peak positions, arising from shifting of the tetragonal reflections to lower Q and expansion of the lattice. The cubic (200) peak at 1.995 \AA^{-1} is also present as early as 40 ps, clearly visible in Figure 5c as a relative increase in scattering intensity between the two tetragonal peaks. This expanded tetragonal/pseudocubic structure per-

sists until 160 – 200 ps, observed as a plateau in the kinetic traces between ~ 80 and ~ 200 ps (Figure 5d). After this initial distortion, the positive tetragonal (004) feature disappears, attributed to polaron dissipation, and the cubic (200) feature grows in further up to ~ 1 ns ($\tau = 250 \pm 400$ ps), indicating a contraction of the structure along the c -axis attributed to continued transition to the pseudocubic phase.²¹

After 1 ns (Figure 5b,e), the TRXRD patterns begin to recover, suggesting that the NCs begin to evolve back toward their original structure. Although initially there is the comparatively rapid recovery of the negative (220) tetragonal peak at 2.009 \AA^{-1} (1 – 20 ns), the positive cubic (200) feature recovers significantly faster. We find that, at late times, $S(t)$ is largely dominated by a long-lived expanded (220) tetragonal feature ($\tau = 617 \pm 1295$ ns), readily apparent in the 200 ns trace of Figure 5c. Within the measured 4 μ s time window, there is near complete return of the transient signal to baseline, from which we can infer recovery of the original structure and reversibility of the lattice distortions.

The TRXRD responses observed here over a range of excitation fluences and delay times indicate rearrangements of multiple structural parameters in response to above bandgap excitation. Given the excess thermal energy present in the system and proximity of a thermally accessible phase transition, we do not completely rule out some thermal contribution to the photoinduced response;¹⁹ however, it is clear that electronic effects play a critical role and that heating of NCs

via photoexcitation cannot adequately explain the observed structural distortions. Under lower fluence excitation conditions ($0.02\text{--}0.34\text{ mJ/cm}^2$), structural rearrangement toward the cubic phase within the first 200 ps is consistent with modest heating of the NCs below the phase transition temperature, as well as experimental and theoretical arguments that photoexcitation can trigger rotation of the $[\text{PbI}_6]^{4-}$ octahedra from tetragonal to cubic orientation via breaking of the MA–I hydrogen bonds.^{14,16,17} Prior work by Wu et al.⁴³ on MAPbI₃ films utilizing ultrafast electron diffraction (UED) also identified a decrease in the Bragg peak intensity occurring within ~ 10 ps following photoexcitation, attributed to the disordering of the lattice associated with rotation of the lead iodide octahedra. Our results similarly show that the integrated $\Delta S(t)$ for each reflection is negative (Figure S16), and the fine Q-resolution in our setup also resolves the emergence of a pseudocubic structure.

At the higher fluences ($>0.34\text{ mJ/cm}^2$) and correspondingly high carrier densities, nonthermal structural elongation develops along the *c*-axis at early time (200 ps), in addition to the pseudocubic structure. We attribute this to a distortion associated with a high concentration of electron polarons. Polaron formation is known to occur via Fröhlich coupling along phonon modes with strong carrier coupling,^{44,45} and in MAPbI₃, the strongest electron–phonon coupling associated with polaron formation occurs along an I–Pb–I *c*-axis stretching mode and an I–Pb–I bending mode, which elongate the *c*-axis and decrease the bond angles of the equatorial atoms.^{12,42,46}

The second stage of growth of the cubic (200) peak observed in the dynamics measurements between ~ 160 ps and 1 ns signals a continued transition to the pseudocubic structure. Interestingly, the polaron feature disappears over the same time frame, consistent with observations by Guzelturk et al. of polaron dissipation in MAPbBr₃ occurring over hundreds of picoseconds.²¹ The continued growth of the cubic (200) peak over this time frame is likely due in part to the dissipation of the polaron, which enables relaxation of the structure along the *c*-axis. Additional heat deposition into the lattice via Auger recombination over this time frame could also be a contributing factor. The Auger recombination lifetime in MAPbI₃ NCs has previously been reported⁴⁷ to be several hundred picoseconds for NCs of diameter 10–25 nm, and although our NCs are larger and might therefore be expected to exhibit a longer Auger lifetime, the higher fluence in our experiments would account for the shorter time constant observed here.

Recovery from the pseudocubic to the tetragonal phase occurs in two stages, and the loss of intensity of the $\Delta S(t)$ cubic (200) peak can be approximated with a biexponential function. The first stage of recovery proceeds with a decay constant of $\tau = 67 \pm 36$ ns that is similar to previously measured radiative recombination lifetimes for bimolecular and monomolecular recombination in MAPbI₃ NCs, ranging from tens to hundreds of nanoseconds.^{47–49} Given that photoexcitation can induce a transition from tetragonal to pseudocubic phase, carrier recombination likely plays a role in reversing the phase transition as well.

The second recovery stage occurs over much longer time scales ($\tau = 617 \pm 1295$ ns), which is subsequent to expected carrier recombination or thermal dissipation times for inorganic semiconductor NCs (on the order of hundreds of picoseconds to nanoseconds),^{11,50} but similar to low temper-

ature tetragonal to orthorhombic phase transition recovery times observed in MAPbI₃ films, suggesting that the slow recovery corresponds to the reverse phase transition to tetragonal symmetry.⁵¹ Ionic transport, which is also a slow process, likely would not result in the emergent cubic signals observed here but rather a long-lived disordering signal. There is also the apparent anisotropy of the recovery to consider, where by 200 ns the tetragonal (004) and cubic (200) peaks have largely recovered but a slightly shifted tetragonal (220) peak remains with greater prominence (Figure 5c). This would suggest a partial recovery of the octahedral rotation—enough to break the cubic symmetry along the *c*-axis; however, full recovery along the equatorial planes does not occur until later. Metastable states have been implicated in bulk MAPbI₃ to account for changes in physical and optical properties after prolonged exposure to light, such as quenched photoluminescence⁵² and increased dielectric constant.⁵³

Mechanistically it is relevant to compare the observed behavior in MAPbI₃ NCs with that of CsPbBr₃ NCs, previously reported in the literature.^{11,19,54} Analogous experiments on CsPbBr₃ NCs by Kirschner et al. identified a photoinduced distortion attributed to an orthorhombic to cubic transition, distinct from a strictly thermal phase transition in that it bypassed the tetragonal phase and the reverse cubic to orthorhombic transition occurred at a much higher temperature than the orthorhombic thermal transition.¹¹ More recently, Cannelli et al. found using transient X-ray absorption spectroscopy (XAS) that a polaronic distortion is likely responsible for much of the structural rearrangement in CsPbBr₃.¹⁹ In MAPbI₃ NCs, we see evidence of both a transition toward the cubic phase and a polaronic distortion, although there are lattice dynamics occurring at time scales significantly longer than those observed for CsPbBr₃. In CsPbBr₃, the lattice distortions detected with TRXRD and XAS reached a maximum within the ~ 80 ps instrument response time and the majority of the recovery occurred within 1 ns. In MAPbI₃, the polaron distortion follows similar dynamics; however, the transient cubic peak reaches a maximum at 1 ns (after the polaron dissipation) and fully recovers only after several microseconds.

The long lattice recovery time we find for MAPbI₃ NCs is an interesting point of comparison to the fully inorganic perovskite NCs.^{11,19} On the contrary, the thermal accessibility of the cubic phase in the case of MAPbI₃ may require more complete particle cooling to revert back to the higher symmetry structure. It is also possible that the interaction between the organic and inorganic lattices presents an energetic barrier for recovery of the tetragonal phase. In the ground state, MA–I hydrogen bonds promote octahedral tilting; however, these are weakened upon population of the conduction band, which shifts the electron density away from I 5p orbitals and toward Pb 6p orbitals.^{14,15} The cubic configuration is energetically favored in the absence of the MA–I hydrogen bonding,¹⁷ which could inhibit reentry to the tetragonal phase even after particle cooling and charge recombination have occurred. Looking forward, theoretical work such as MD simulations could aid in further elucidating the underlying mechanisms. Continued ultrafast studies could also be fruitful, especially comparing band gap with above band gap excitation energies, which could aid in separating contributions from phase-related structural changes, polaron formation, and thermal effects.

CONCLUSIONS

In summary, variable temperature XRD identifies the tetragonal to cubic phase transition in MAPbI₃ NCs at temperatures as low as 50 °C. Fluence-dependent TRXRD measurements have further discerned that photoexcitation can transiently induce a reversible phase transition to a pseudocubic phase. TRXRD measurements identify the initial material response to photoexcitation is lattice expansion in the tetragonal phase assisted by polaron formation that subsequently undergoes transition to the pseudocubic phase. Further transformation from the tetragonal to cubic structure occurs upon polaron dissipation, likely thermally assisted via Auger recombination over ~ 1 ns. Recovery of tetragonal symmetry occurs over tens of nanoseconds, correlated with the radiative recombination lifetime of the charge carriers and thermal cooling; however, a metastable phase with expanded structure along the tetragonal *a*- and *b*-axes persists for several microseconds before full recovery of the ambient phase. The transient nature of this phase transformation occurring over multiple stages is of significance to lasing or concentrated solar applications, which expose active materials to high fluence excitation and may rely on specific optoelectronic properties that are subject to change with the crystal phase. This study illustrates the long-lived structural effects of photoexcitation on the crystal lattice, as well as an unexpected metastability likely associated with overall comparable thermodynamic energies of tetragonal and cubic crystal phases.

METHODS

Synthesis of Materials. Lead iodide (99.999%), methylammonium iodide (98%), methylamine (2 M in THF), formamidine acetate (99%), oleylamine (70%), oleic acid (90%), octadecene (90%), and dimethylformamide (anhydrous, 99.8%) were purchased from Sigma-Aldrich. Oleylamine and oleic acid were dried under a vacuum at 100 °C and stored in a nitrogen glovebox before use.

MAPbI₃ NCs were synthesized using a modified version of the procedure described in Vybornyi et al., modified to increase the scale of the reaction.⁹ Following a 6 \times scaleup, 522 mg of lead iodide and 30 mL of ODE were loaded into a 50 mL three-neck flask and heated under a vacuum to 120 °C and held 1 h. Under nitrogen, 3 mL of dry oleylamine and 3 mL of dry oleic acid were injected into the reaction flask, which was stirred under nitrogen until the lead iodide dissolved completely, leaving a yellow solution. Then, the reaction was set to the injection temperature of 60 °C. Under nitrogen, an injection was rapidly made with 1.02 mL of 2 M methylamine solution in THF mixed with 4 mL of dry oleic acid. The reaction was cooled with a water bath after 5 s. The crude reaction product was then centrifuged at 12 000 rpm to isolate a brown precipitate that was redispersed in dodecane for optical and X-ray experiments.

Variable Temperature X-ray Diffraction. Variable temperature X-ray diffraction measurements were performed at Sector 5 DND-CAT at the Advanced Photon Source (APS) at Argonne National Laboratory. Colloidal NC suspensions in dodecane were prepared in flame-sealed glass capillaries and the temperature was ramped in 25 °C increments from 25 to 175 °C. Incident X-ray pulses were at 11.7 keV, and XRD patterns were collected on a Pilatus detector and then azimuthally integrated. Ten 1 s X-ray exposures were collected and averaged together for presented data.

Time-Resolved X-ray Diffraction. Transient X-ray diffraction experiments were performed at Sector 11-ID-D of the Advanced Photon Source. The pump pulse was produced by a Ti:sapphire regenerative amplified laser (Coherent Legend Elite Duo) seeded by a Micra-5 oscillator and pumped by an Evolution intracavity-doubled, diode-pumped ND:YLF Q-switched laser. The 800 nm output was then frequency doubled using a BBO crystal to generate 400 nm optical pulses with 10 kHz repetition rate and 1.6 ps fwhm. The X-ray

probe pulses had an energy of 11.7 keV with ~ 79 ps pulse width. The pump and probe beams were made to overlap on the perovskite nanocrystal sample dispersion, which was rapidly flowed as a degassed 0.76 mm diameter laminar jet to provide fresh material for optical excitation. Dodecane was chosen as the solvent for its high sample stability and low volatility. Powder diffraction patterns were collected on a Dectris Pilatus 2M detector.

Powder diffraction patterns were processed using QXRD software and home-built Matlab programs. Ab initio structure solutions, which would typically be used for crystal indexing and space-group determination, present challenges for nanocrystalline materials due to line broadening of diffraction peaks. This method would prove especially difficult for TRXRD experiments, where the small excitation fraction produces only subtle changes in the XRD patterns against a backdrop of unexcited material. We therefore have opted to analyze TRXRD data as difference patterns, subtracting the pre-time zero pattern from the post-time zero pattern, to visualize light-induced changes to the structure.

ASSOCIATED CONTENT

Supporting Information

The Supporting Information is available free of charge at <https://pubs.acs.org/doi/10.1021/acsnano.2c06950>.

Figures of temperature cycling of NCs, ΔS patterns resulting from peak shifting or loss of peak intensity, pre-time zero static diffraction patterns, percent loss per minute of static X-ray diffraction peak intensity versus excitation fluence, fluence dependence of transient scattering versus *Q*, kinetic traces of TRXRD peaks and associated lifetimes, discussions of TRXRD experimental details, size estimation of NCs, variable temperature XRD data processing, TRXRD data processing and degradation correction, TRXRD fluence dependence, TRXRD dynamics analysis, estimation of laser-induced temperature changes, and tables of NC particle diameter calculation, summary of growth and recovery time constants (PDF)

AUTHOR INFORMATION

Corresponding Author

Richard D. Schaller – Department of Chemistry, Northwestern University, Evanston, Illinois 60208, United States; Center for Nanoscale Materials, Argonne National Laboratory, Lemont, Illinois 60439, United States; Institute for Sustainability and Energy at Northwestern, Northwestern University, Evanston, Illinois 60208, United States; orcid.org/0000-0001-9696-8830; Email: Schaller@anl.gov

Authors

Ariel A. Leonard – Department of Chemistry, Northwestern University, Evanston, Illinois 60208, United States

Benjamin T. Diroll – Center for Nanoscale Materials, Argonne National Laboratory, Lemont, Illinois 60439, United States; orcid.org/0000-0003-3488-0213

Nathan C. Flanders – Department of Chemistry, Northwestern University, Evanston, Illinois 60208, United States; Present Address: Institute for Integrated Cell Material Sciences, Kyoto University, Kyoto, 606-8501, Japan

Shobhana Panuganti – Department of Chemistry, Northwestern University, Evanston, Illinois 60208, United States; orcid.org/0000-0003-1762-527X

Alexandra Brumberg – Department of Chemistry, Northwestern University, Evanston, Illinois 60208, United States; Present Address: Materials Research Laboratory, University of California, Santa Barbara, 93106, United States; orcid.org/0000-0003-2512-4686

Matthew S. Kirschner – Department of Chemistry, Northwestern University, Evanston, Illinois 60208, United States

Shelby A. Cuthriell – Department of Chemistry, Northwestern University, Evanston, Illinois 60208, United States

Samantha M. Harvey – Department of Chemistry, Northwestern University, Evanston, Illinois 60208, United States; Present Address: Department of Chemistry, University of Washington, Seattle, 98195, United States

Nicolas E. Watkins – Department of Chemistry, Northwestern University, Evanston, Illinois 60208, United States; orcid.org/0000-0002-0417-7909

Jin Yu – X-ray Sciences Division, Argonne National Laboratory, Lemont, Illinois 60439, United States

Michael R. Wasielewski – Department of Chemistry, Northwestern University, Evanston, Illinois 60208, United States; Institute for Sustainability and Energy at Northwestern, Northwestern University, Evanston, Illinois 60208, United States; orcid.org/0000-0003-2920-5440

Mercouri G. Kanatzidis – Department of Chemistry, Northwestern University, Evanston, Illinois 60208, United States; orcid.org/0000-0003-2037-4168

William R. Dichtel – Department of Chemistry, Northwestern University, Evanston, Illinois 60208, United States; orcid.org/0000-0002-3635-6119

Xiaoyi Zhang – X-ray Sciences Division, Argonne National Laboratory, Lemont, Illinois 60439, United States; orcid.org/0000-0001-9732-1449

Lin X. Chen – Department of Chemistry, Northwestern University, Evanston, Illinois 60208, United States; Chemical Sciences and Engineering Division, Argonne National Laboratory, Lemont, Illinois 60439, United States; orcid.org/0000-0002-8450-6687

Complete contact information is available at:
<https://pubs.acs.org/10.1021/acsnano.2c06950>

Author Contributions

The manuscript was written through contributions of all authors. All authors have given approval to the final version of the manuscript.

Notes

The authors declare no competing financial interest.

ACKNOWLEDGMENTS

The authors acknowledge support from the Ultrafast Initiative of the U.S. Department of Energy, Office of Science, Office of Basic Energy Sciences, through Argonne National Laboratory under Contract No. DE-AC02-06CH11357. The authors acknowledge support from the National Science Foundation MSN under grant 1808590. This material is based upon work supported by the National Science Foundation Graduate Student Fellowship Program under Grant No. DGE-1842165 (S.P., A.B., S.M.H., and N.E.W.). S.M.H. and M.R.W. were supported by the Office of Science, Office of Basic Energy Sciences, Department of Energy under award DE-FG02-99ER14999. Work performed at the Center for Nanoscale Materials and Advanced Photon Source, both U.S. Department

of Energy Office of Science User Facilities, was supported by the U.S. DOE, Office of Basic Energy Sciences, under Contract No. DE-AC02-06CH11357. The submitted manuscript was created by UChicago Argonne, LLC, Operator of Argonne National Laboratory ("Argonne"). Argonne, a U.S. Department of Energy Office of Science laboratory, is operated under Contract No. DE-AC02-06CH11357. The U.S. Government retains for itself, and others acting on its behalf, a paid-up nonexclusive, irrevocable worldwide license in said article to reproduce, prepare derivative works, distribute copies to the public, and perform publicly and display publicly, by or on behalf of the Government. The Department of Energy will provide public access to these results of federally sponsored research in accordance with the DEO Public Access Plan: <http://energy.gov/downloads/doe-public-access-plan>.

ABBREVIATIONS USED

XRD, X-ray diffraction; TRXRD, transient X-ray diffraction; NC, nanocrystal

REFERENCES

- (1) Huang, H.; Polavarapu, L.; Sichert, J. A.; Susa, A. S.; Urban, A. S.; Rogach, A. L. Colloidal Lead Halide Perovskite Nanocrystals: Synthesis, Optical Properties and Applications. *NPG Asia Mater.* **2016**, *8*, e328–e328.
- (2) Dey, A.; Ye, J.; De, A.; Debroye, E.; Ha, S. K.; Bladt, E.; Kshirsagar, A. S.; Wang, Z.; Yin, J.; Wang, Y.; Quan, L. N.; Yan, F.; Gao, M.; Li, X.; Shamsi, J.; Debnath, T.; Cao, M.; Scheel, M. A.; Kumar, S.; Steele, J. A.; et al. State of the Art and Prospects for Halide Perovskite Nanocrystals. *ACS Nano* **2021**, *15*, 10775–10981.
- (3) Choi, J. J.; Yang, X.; Norman, Z. M.; Billinge, S. J.; Owen, J. S. Structure of Methylammonium Lead Iodide within Mesoporous Titanium Dioxide: Active Material in High-Performance Perovskite Solar Cells. *Nano Lett.* **2014**, *14*, 127–133.
- (4) Oga, H.; Saeki, A.; Ogomi, Y.; Hayase, S.; Seki, S. Improved Understanding of the Electronic and Energetic Landscapes of Perovskite Solar Cells: High Local Charge Carrier Mobility, Reduced Recombination, and Extremely Shallow Traps. *J. Am. Chem. Soc.* **2014**, *136*, 13818–13825.
- (5) Ponseca, C. S., Jr.; Savenije, T. J.; Abdellah, M.; Zheng, K.; Yartsev, A.; Pascher, T.; Harlang, T.; Chabera, P.; Pullerits, T.; Stepanov, A.; Wolf, J. P.; Sundstrom, V. Organometal Halide Perovskite Solar Cell Materials Rationalized: Ultrafast Charge Generation, High and Microsecond-Long Balanced Mobilities, and Slow Recombination. *J. Am. Chem. Soc.* **2014**, *136*, 5189–5192.
- (6) Fu, H. Colloidal Metal Halide Perovskite Nanocrystals: A Promising Juggernaut in Photovoltaic Applications. *J. Mater. Chem. A* **2019**, *7*, 14357–14379.
- (7) Xing, G.; Mathews, N.; Sun, S.; Lim, S. S.; Lam, Y. M.; Gratzel, M.; Mhaisalkar, S.; Sum, T. C. Long-Range Balanced Electron- and Hole-Transport Lengths in Organic-Inorganic $\text{CH}_3\text{NH}_3\text{PbI}_3$. *Science* **2013**, *342*, 344.
- (8) Protesescu, L.; Yakunin, S.; Bodnarchuk, M. I.; Krieg, F.; Caputo, R.; Hendon, C. H.; Yang, R. X.; Walsh, A.; Kovalenko, M. V. Nanocrystals of Cesium Lead Halide Perovskites (CsPbX_3 , X = Cl, Br, and I): Novel Optoelectronic Materials Showing Bright Emission with Wide Color Gamut. *Nano Lett.* **2015**, *15*, 3692–3696.
- (9) Vybornyi, O.; Yakunin, S.; Kovalenko, M. V. Polar-Solvent-Free Colloidal Synthesis of Highly Luminescent Alkylammonium Lead Halide Perovskite Nanocrystals. *Nanoscale* **2016**, *8*, 6278–6283.
- (10) De Giorgi, M. L.; Anni, M. Amplified Spontaneous Emission and Lasing in Lead Halide Perovskites: State of the Art and Perspectives. *Appl. Sci.* **2019**, *9*, 4591.
- (11) Kirschner, M. S.; Diroll, B. T.; Guo, P.; Harvey, S. M.; Helweh, W.; Flanders, N. C.; Brumberg, A.; Watkins, N. E.; Leonard, A. A.; Evans, A. M.; Wasielewski, M. R.; Dichtel, W. R.; Zhang, X.; Chen, L.

- X.; Schaller, R. D. Photoinduced, Reversible Phase Transitions in All-Inorganic Perovskite Nanocrystals. *Nat. Commun.* **2019**, *10*, 504.
- (12) Ghosh, D.; Welch, E.; Neukirch, A. J.; Zakhidov, A.; Tretiak, S. Polarons in Halide Perovskites: A Perspective. *J. Phys. Chem. Lett.* **2020**, *11*, 3271–3286.
- (13) Herz, L. M. Charge-Carrier Dynamics in Organic-Inorganic Metal Halide Perovskites. *Annu. Rev. Phys. Chem.* **2016**, *67*, 65–89.
- (14) Zhou, Y.; You, L.; Wang, S.; Ku, Z.; Fan, H.; Schmidt, D.; Rusydi, A.; Chang, L.; Wang, L.; Ren, P.; Chen, L.; Yuan, G.; Chen, L.; Wang, J. Giant Photostriction in Organic-Inorganic Lead Halide Perovskites. *Nat. Commun.* **2016**, *7*, 11193.
- (15) Umebayashi, T.; Asai, K.; Kondo, T.; Nakao, A. Electronic Structures of Lead Iodide Based Low-Dimensional Crystals. *Phys. Rev. B* **2003**, *67*, 155405.
- (16) Lee, J. H.; Bristowe, N. C.; Bristowe, P. D.; Cheetham, A. K. Role of Hydrogen-Bonding and Its Interplay with Octahedral Tilting in $\text{CH}_3\text{NH}_3\text{PbI}_3$. *Chem. Commun.* **2015**, *51*, 6434–6437.
- (17) Lee, J.-H.; Bristowe, N. C.; Lee, J. H.; Lee, S.-H.; Bristowe, P. D.; Cheetham, A. K.; Jang, H. M. Resolving the Physical Origin of Octahedral Tilting in Halide Perovskites. *Chem. Mater.* **2016**, *28*, 4259–4266.
- (18) Miyata, K.; Meggiolaro, D.; Trinh, M. T.; Joshi, P. P.; Mosconi, E.; Jones, S. C.; De Angelis, F.; Zhu, X. Y. Large Polarons in Lead Halide Perovskites. *Sci. Adv.* **2017**, *3*, e1701217.
- (19) Cannelli, O.; Colonna, N.; Puppini, M.; Rossi, T. C.; Kinschel, D.; Leroy, L. M. D.; Löffler, J.; Budarz, J. M.; March, A. M.; Doumy, G.; Al Haddad, A.; Tu, M. F.; Kumagai, Y.; Walko, D.; Smolentsev, G.; Krieg, F.; Boehme, S. C.; Kovalenko, M. V.; Chergui, M.; Mancini, G. F. Quantifying Photoinduced Polaronic Distortions in Inorganic Lead Halide Perovskite Nanocrystals. *J. Am. Chem. Soc.* **2021**, *143*, 9048–9059.
- (20) Zhu, H.; Miyata, K.; Fu, Y.; Wang, J.; Joshi, P. P.; Niesner, D.; Williams, K. W.; Jin, S.; Zhu, X.-Y. Screening in Crystalline Liquids Protects Energetic Carriers in Hybrid Perovskites. *Science* **2016**, *353*, 1409.
- (21) Guzelturk, B.; Winkler, T.; Van de Goor, T. W. J.; Smith, M. D.; Bourelle, S. A.; Feldmann, S.; Trigo, M.; Teitelbaum, S. W.; Steinruck, H. G.; de la Pena, G. A.; Alonso-Mori, R.; Zhu, D.; Sato, T.; Karunadasa, H. I.; Toney, M. F.; Deschler, F.; Lindenberg, A. M. Visualization of Dynamic Polaronic Strain Fields in Hybrid Lead Halide Perovskites. *Nat. Mater.* **2021**, *20*, 618–623.
- (22) Wu, X.; Tan, L. Z.; Shen, X.; Hu, T.; Miyata, K.; Trinh, M. T.; Li, R.; Coffee, R.; Liu, S.; Egger, D. A.; Makasyuk, I.; Zheng, Q.; Fry, A.; Robinson, J. S.; Smith, M. D.; Guzelturk, B.; Karunadasa, H. I.; Wang, X.; Zhu, X.; Kronik, L.; et al. Light-Induced Picosecond Rotational Disorder of the Inorganic Sublattice in Hybrid Perovskites. *Sci. Adv.* **2017**, *3*, No. e1602388.
- (23) Meggiolaro, D.; Ambrosio, F.; Mosconi, E.; Mahata, A.; De Angelis, F. Polarons in Metal Halide Perovskites. *Adv. Energy Mater.* **2020**, *10*, 1902748.
- (24) Seiler, H.; Palato, S.; Sonnichsen, C.; Baker, H.; Socie, E.; Strandell, D. P.; Kambhampati, P. Two-Dimensional Electronic Spectroscopy Reveals Liquid-Like Lineshape Dynamics in CsPbI_3 Perovskite Nanocrystals. *Nat. Commun.* **2019**, *10*, 4962.
- (25) Zhu, X. Y.; Podzorov, V. Charge Carriers in Hybrid Organic-Inorganic Lead Halide Perovskites Might Be Protected as Large Polarons. *J. Phys. Chem. Lett.* **2015**, *6*, 4758–4761.
- (26) Makarov, N. S.; Guo, S.; Isaienko, O.; Liu, W.; Robel, I.; Klimov, V. I. Spectral and Dynamical Properties of Single Excitons, Biexcitons, and Trions in Cesium-Lead-Halide Perovskite Quantum Dots. *Nano Lett.* **2016**, *16*, 2349–2362.
- (27) Baikie, T.; Fang, Y.; Kadro, J. M.; Schreyer, M.; Wei, F.; Mhaisalkar, S. G.; Graetzel, M.; White, T. J. Synthesis and Crystal Chemistry of the Hybrid Perovskite $\text{CH}_3\text{NH}_3\text{PbI}_3$ for Solid-State Sensitized Solar Cell Applications. *J. Mater. Chem. A* **2013**, *1*, 5628.
- (28) Mashiyama, H.; Kurihara, Y.; Azetsu, T. Disordered Cubic Perovskite Structure of $\text{CH}_3\text{NH}_3\text{PbX}_3$ ($\text{X} = \text{Cl}, \text{Br}, \text{I}$). *J. Korean Phys. Soc.* **1998**, *32*, S156–S158.
- (29) Whitfield, P. S.; Herron, N.; Guise, W. E.; Page, K.; Cheng, Y. Q.; Milas, I.; Crawford, M. K. Structures, Phase Transitions and Tricritical Behavior of the Hybrid Perovskite Methyl Ammonium Lead Iodide. *Sci. Rep.* **2016**, *6*, 35685.
- (30) Pisoni, A.; Jacimovic, J.; Barisic, O. S.; Spina, M.; Gaal, R.; Forro, L.; Horvath, E. Ultra-Low Thermal Conductivity in Organic-Inorganic Hybrid Perovskite $\text{CH}_3\text{NH}_3\text{PbI}_3$. *J. Phys. Chem. Lett.* **2014**, *5*, 2488–2492.
- (31) Ge, C.; Hu, M.; Wu, P.; Tan, Q.; Chen, Z.; Wang, Y.; Shi, J.; Feng, J. Ultralow Thermal Conductivity and Ultrahigh Thermal Expansion of Single-Crystal Organic-Inorganic Hybrid Perovskite $\text{CH}_3\text{NH}_3\text{PbX}_3$ ($\text{X} = \text{Cl}, \text{Br}, \text{I}$). *J. Phys. Chem. C* **2018**, *122*, 15973–15978.
- (32) Kovalsky, A.; Wang, L.; Marek, G. T.; Burda, C.; Dyck, J. S. Thermal Conductivity of $\text{CH}_3\text{NH}_3\text{PbI}_3$ and CsPbI_3 : Measuring the Effect of the Methylammonium Ion on Phonon Scattering. *J. Phys. Chem. C* **2017**, *121*, 3228–3233.
- (33) Yi, H. T.; Wu, X.; Zhu, X.; Podzorov, V. Intrinsic Charge Transport across Phase Transitions in Hybrid Organo-Inorganic Perovskites. *Adv. Mater.* **2016**, *28*, 6509–6514.
- (34) Diroll, B. T. Temperature-Dependent Intraband Relaxation of Hybrid Perovskites. *J. Phys. Chem. Lett.* **2019**, *10*, 5623–5628.
- (35) Guzelturk, B.; Cotts, B. L.; Jasrasaria, D.; Philbin, J. P.; Hanifi, D. A.; Koscher, B. A.; Balan, A. D.; Curling, E.; Zajac, M.; Park, S.; Yazdani, N.; Nyby, C.; Kamysbayev, V.; Fischer, S.; Nett, Z.; Shen, X.; Kozina, M. E.; Lin, M. F.; Reid, A. H.; Weathersby, S. P.; et al. Dynamic Lattice Distortions Driven by Surface Trapping in Semiconductor Nanocrystals. *Nat. Commun.* **2021**, *12*, 1860.
- (36) Stoumpos, C. C.; Malliakas, C. D.; Kanatzidis, M. G. Semiconducting Tin and Lead Iodide Perovskites with Organic Cations: Phase Transitions, High Mobilities, and Near-Infrared Photoluminescent Properties. *Inorg. Chem.* **2013**, *52*, 9019–9038.
- (37) Groom, C. R.; Bruno, I. J.; Lightfoot, M. P.; Ward, S. C. The Cambridge Structural Database. *Acta Crystallogr., Sect. B: Struct. Sci., Cryst. Eng. Mater.* **2016**, *72*, 171–179.
- (38) Sewvandi, G. A.; Hu, D.; Chen, C.; Ma, H.; Kusunose, T.; Tanaka, Y.; Nakanishi, S.; Feng, Q. Antiferroelectric-to-Ferroelectric Switching in $\text{CH}_3\text{NH}_3\text{PbI}_3$ Perovskite and Its Potential Role in Effective Charge Separation in Perovskite Solar Cells. *Phys. Rev. Appl.* **2016**, *6*, 024007.
- (39) Kawamura, Y.; Mashiyama, H.; Hasebe, K. Structural Study on Cubic-Tetragonal Transition of $\text{CH}_3\text{NH}_3\text{PbI}_3$. *J. Phys. Soc. Jpn.* **2002**, *71*, 1694–1697.
- (40) Cannelli, O.; Wiktor, J.; Colonna, N.; Leroy, L.; Puppini, M.; Bacellar, C.; Sadykov, I.; Krieg, F.; Smolentsev, G.; Kovalenko, M. V.; Pasquarello, A.; Chergui, M.; Mancini, G. F. Atomic-Level Description of Thermal Fluctuations in Inorganic Lead Halide Perovskites. *J. Phys. Chem. Lett.* **2022**, *13*, 3382–3391.
- (41) Momma, K.; Izumi, F. VESTA 3 for Three-Dimensional Visualization of Crystal, Volumetric and Morphology Data. *J. Appl. Crystallogr.* **2011**, *44*, 1272–1276.
- (42) Park, M.; Neukirch, A. J.; Reyes-Lillo, S. E.; Lai, M.; Ellis, S. R.; Dietze, D.; Neaton, J. B.; Yang, P.; Tretiak, S.; Mathies, R. A. Excited-State Vibrational Dynamics toward the Polaron in Methylammonium Lead Iodide Perovskite. *Nat. Commun.* **2018**, *9*, 2525.
- (43) Wu, X.; Tan, L. Z.; Shen, X.; Hu, T.; Miyata, K.; Trinh, M. T.; Li, R.; Coffee, R.; Liu, S.; Egger, D. A.; Makasyuk, I.; Zheng, Q.; Fry, A.; Robinson, J. S.; Smith, M. D.; Guzelturk, B.; Karunadasa, H. I.; Wang, X.; Zhu, X.; Kronik, L.; et al. Light-Induced Picosecond Rotational Disorder of the Inorganic Sublattice in Hybrid Perovskites. *Sci. Adv.* **2017**, *3*, No. e1602388.
- (44) Batignani, G.; Fumero, G.; Srimath Kandada, A. R.; Cerullo, G.; Gandini, M.; Ferrante, C.; Petrozza, A.; Scopigno, T. Probing Femtosecond Lattice Displacement Upon Photo-Carrier Generation in Lead Halide Perovskite. *Nat. Commun.* **2018**, *9*, 1971.
- (45) Puppini, M.; Polishchuk, S.; Colonna, N.; Crepaldi, A.; Dirin, D. N.; Nazarenko, O.; De Gennaro, R.; Gatti, G.; Roth, S.; Barillot, T.; Poletto, L.; Xian, R. P.; Rettig, L.; Wolf, M.; Ernstorfer, R.; Kovalenko, M. V.; Marzari, N.; Grioni, M.; Chergui, M. Evidence of Large

Polarons in Photoemission Band Mapping of the Perovskite Semiconductor CsPbBr₃. *Phys. Rev. Lett.* **2020**, *124*, 206402.

(46) Schlipf, M.; Ponce, S.; Giustino, F. Carrier Lifetimes and Polaronic Mass Enhancement in the Hybrid Halide Perovskite CH₃NH₃PbI₃ from Multiphonon Frohlich Coupling. *Phys. Rev. Lett.* **2018**, *121*, 086402.

(47) Eperon, G. E.; Jedlicka, E.; Ginger, D. S. Biexciton Auger Recombination Differs in Hybrid and Inorganic Halide Perovskite Quantum Dots. *J. Phys. Chem. Lett.* **2018**, *9*, 104–109.

(48) Jang, D. M.; Park, K.; Kim, D. H.; Park, J.; Shojaei, F.; Kang, H. S.; Ahn, J.-P.; Lee, J. W.; Song, J. K. Reversible Halide Exchange Reaction of Organometal Trihalide Perovskite Colloidal Nanocrystals for Full-Range Band Gap Tuning. *Nano Lett.* **2015**, *15*, 5191–5199.

(49) Hassan, Y.; Ashton, O. J.; Park, J. H.; Li, G.; Sakai, N.; Wenger, B.; Haghighirad, A. A.; Noel, N. K.; Song, M. H.; Lee, B. R.; Friend, R. H.; Snaith, H. J. Facile Synthesis of Stable and Highly Luminescent Methylammonium Lead Halide Nanocrystals for Efficient Light Emitting Devices. *J. Am. Chem. Soc.* **2019**, *141*, 1269–1279.

(50) Harvey, S. M.; Houck, D. W.; Kirschner, M. S.; Flanders, N. C.; Brumberg, A.; Leonard, A. A.; Watkins, N. E.; Chen, L. X.; Dichtel, W. R.; Zhang, X.; Korgel, B. A.; Wasielewski, M. R.; Schaller, R. D. Transient Lattice Response Upon Photoexcitation in CuInSe₂ Nanocrystals with Organic or Inorganic Surface Passivation. *ACS Nano* **2020**, *14*, 13548–13556.

(51) Li, S.; Dai, Z.; Kocoj, C. A.; Altman, E. I.; Padture, N. P.; Guo, P. Photothermally Induced, Reversible Phase Transition in Methylammonium Lead Triiodide. *Matter* **2023**, *6*, 460.

(52) Gottesman, R.; Gouda, L.; Kalanoor, B. S.; Haltzi, E.; Tirosh, S.; Rosh-Hodesh, E.; Tischler, Y.; Zaban, A.; Quarti, C.; Mosconi, E.; De Angelis, F. Photoinduced Reversible Structural Transformations in Free-Standing CH₃NH₃PbI₃ Perovskite Films. *J. Phys. Chem. Lett.* **2015**, *6*, 2332–2338.

(53) Nie, W.; Blancon, J. C.; Neukirch, A. J.; Appavoo, K.; Tsai, H.; Chhowalla, M.; Alam, M. A.; Sfeir, M. Y.; Katan, C.; Even, J.; Tretiak, S.; Crochet, J. J.; Gupta, G.; Mohite, A. D. Light-Activated Photocurrent Degradation and Self-Healing in Perovskite Solar Cells. *Nat. Commun.* **2016**, *7*, 11574.

(54) Seiler, H.; Zahn, D.; Taylor, V. C. A.; Bodnarchuk, M. I.; Windsor, Y. W.; Kovalenko, M. V.; Ernstorfer, R. Direct Observation of Ultrafast Lattice Distortions During Exciton-Polaron Formation in Lead Halide Perovskite Nanocrystals. *ACS Nano* **2023**, *17*, 1979–1988.

Recommended by ACS

Controlled Assembly and Anomalous Thermal Expansion of Ultrathin Cesium Lead Bromide Nanoplatelets

Chantalle J. Krajewska, Mouni G. Bawendi, *et al.*

MARCH 08, 2023
NANO LETTERS

READ 

Light-Induced Structural Dynamics and Charge Transport in Layered Halide Perovskite Thin Films

Hsinhan Tsai, Wanyi Nie, *et al.*

JANUARY 05, 2023
NANO LETTERS

READ 

Spacer-Dependent and Pressure-Tuned Structures and Optoelectronic Properties of 2D Hybrid Halide Perovskites

Jesse Ratté, Yang Song, *et al.*

JANUARY 09, 2023
THE JOURNAL OF PHYSICAL CHEMISTRY LETTERS

READ 

Strain-Induced Indirect-to-Direct Bandgap Transition, Photoluminescence Enhancement, and Linewidth Reduction in Bilayer MoTe₂

Yueyang Yu, Cun-Zheng Ning, *et al.*

FEBRUARY 22, 2023
ACS NANO

READ 

Get More Suggestions >